Superconductivity of repulsive spinless fermions with sublattice potentials

Yuchi He,[1] Kang Yang,[2] Jonas B. Hauck,[1] Emil J. Bergholtz,[2] and Dante M. Kennes[1, 3]

[1]*Institut für Theorie der Statistischen Physik, RWTH Aachen University and*
JARA—Fundamentals of Future Information Technology, 52056 Aachen, Germany
[2]*Department of Physics, Stockholm University, AlbaNova University Center, 106 91 Stockholm, Sweden*
[3]*Max Planck Institute for the Structure and Dynamics of Matter,*
Center for Free Electron Laser Science, 22761 Hamburg, Germany
(Dated: August 8, 2022)

We explore unconventional superconductivity of repulsive spinless fermions on square and honeycomb lattices with staggered sublattice potentials. The two lattices can exhibit staggered d-wave and f-wave pairing respectively at low doping stemming from an effective two-valley band structure. At higher doping, in particular the square lattice displays a much richer phase diagram including topological $p + ip$ superconductivity which is induced by a qualitatively different mechanism compared to the d-wave pairing. We illuminate this from several complementary perspectives: we analytically perform sublattice projection to analyze the effective continuum low-energy description and we numerically calculate the binding energies for pair and larger bound states for few-body doping near half filling. Furthermore, for finite doping, we present phase diagrams based on extensive FRG and and DMRG calculations.

There have been substantial efforts [1–4] to understand superconductivity mechanisms beyond the conventional phonon-mediated [5] electron-electron attraction. In one category of mechanisms, bare repulsive electron-electron interaction becomes effectively attractive due to virtual processes after projections to the sublattice or bands [6–8]. Recently, exact results for an effective attraction have been obtained for fermionic honeycomb lattice models with a large staggered sublattice potential [9–11]. This mechanism can be essentially captured by a minimal model of spinless fermions [9], of which the low-energy physics projected to one sublattice shows effective attraction. Such a mechanism has been argued to be relevant for triplet pairing in materials [10, 12–14].

In this Letter, we study the pairing of spinless fermions on the square lattice in addition to the honeycomb lattice model studied in Ref. [9]. Studying a different lattice can shed light on the relevance of the proposed pairing mechanism to layered materials, in which different lattice structures can be realized [15]. Considering a different lattice contributes to further understanding the ingredients of the sublattice projection mechanism for superconductivity—and, as we show, reveals qualitatively new possibilities. The effective theory from a sublattice projection depends on the coordination number of the lattices; lattice symmetry is crucial for the realization of different types of unconventional superconductivity [16–20].

The overall result is summarized in Fig. 1. The quantum phases are inferred through infinite density matrix renormalization group (DMRG) [21, 22] data for strong coupling combined with functional renormalization group (FRG) data at weak coupling [23]. Superconducting phases are found in a wide range of interaction parameters in the honeycomb model while its regime is limited to smaller interaction for the square model. Compared to a previous study [9], a significant difference is that there are two superconducting phases on the square lattice, the

staggered d-wave and the $p+ip$ topological phases, in contrast to the sole f-wave pairing on the honeycomb lattice. The d-wave pairing on the square lattice shares the same origin as the f-wave pairing on the honeycomb lattice in the sense of inter-valley pairing. The Cooper pair arises from an inter-valley attraction revealed by sublattice projection. This requires a next-nearest-neighbor hopping t' to realize two-valley band structure for the square lattice. Upon increasing doping, we observe a transition from staggered d to a topological $p + ip$ [24] superconductor. With zero momentum, $p + ip$ no longer results from the inter-valley attraction. It does not require the next-nearest-neighbor hopping. Moreover, at stronger interactions we find evidence for a transition from superconductivity to inhomogeneous states.

Model and low-energy description.— We use the square lattice as an example while the honeycomb model can be found in Ref. [9]. The Hamiltonian on the square lattice (Fig. 1(a1)) is taken as

$$H = \sum_{\langle i,j \rangle} \left[- \left(t c_i^\dagger c_j + h.c. \right) + V n_i n_j \right]$$
$$- \sum_{\langle\langle i,j \rangle\rangle} \left(t' c_i^\dagger c_j + h.c. \right) + \sum_{i \in B} D n_i, \qquad (1)$$

where c_i, $(c_i^\dagger)$ is the fermionic annihilation (creation) operator on site i, and $n_i = c_i^\dagger c_i$. The symbols $\langle i,j \rangle, \langle\langle i,j \rangle\rangle$ denote nearest neighbors and next-nearest neighbors accordingly. We limit our attention to repulsive interaction $V > 0$ and sublattice potential $D \gg |t| > 0$ on the sublattice B. At half filling and large D, the ground state is expected to have the A sublattice fully filled and the B sublattice unfilled. When $t' = 0$, the Hamiltonian exhibits an explicit symmetry of particle-hole transformation $c_A^\dagger \to c_A$ and $c_B^\dagger \to -c_B$ combined with spatial inversion that interchanges the sublattices. When $t' \neq 0$, the combined particle-hole symmetry equivalently changes the sign of t'.
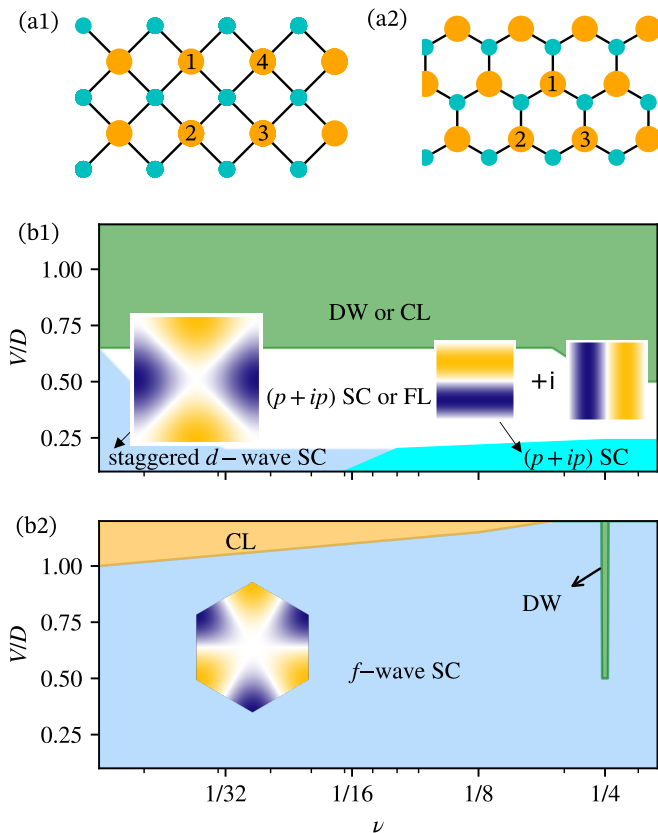
FIG. 1. **Lattice structure and schematic phase diagrams.** (a) Lattice structure for square (a1) and honeycomb (a2) lattice; sublattices are marked in orange and cyan. (b) Phase diagram for square lattice with $t' = \lambda_0$ (b1) and honeycomb lattice (b2) with $t' = 0$, inferred from FRG (weak coupling) and DMRG (strong coupling). For superconducting (SC) phases, we plot the momentum dependence of the susceptibility from FRG. For the $p + ip$ SC, a degenerate pair of dominant eigenvectors is found in FRG, and a mean field analysis indicates the linear combination $p + ip$ is favoured. DW denotes the density wave phase. CL denotes a phase separation via collapse of electrons on the B sublattice. FL denotes Fermi liquids. For the uncertainty in the DMRG data interpretation, see the discussion in the main text.

We focus on electron doping the system above half filling, where the low-energy physics is controlled by those extra electrons on the B lattice. The effective model is derived by a Schrieffer–Wolff transformation [25, 26] (details see the supplement [27]). Up to the second-order of t, this effective Hamiltonian contains terms of hopping, correlated hopping, and interactions: $H_{\text{eff}} = H_{\text{hopping}} + H_{\text{ch}} + H_U$.

Different parts of the Hamiltonian are introduced as follows, while the details of the coefficients see the supplement [27]. H_{hopping} contains nearest neighbors $\langle ij \rangle$ and next-nearest neighbors $\langle\langle ij \rangle\rangle$ terms for the sublattice B:

$$H_{\text{hopping}} = \left[\sum_{\langle ij \rangle} t_B c_{i,B}^\dagger c_{j,B} + \sum_{\langle\langle ij \rangle\rangle} t'_B c_{i,B}^\dagger c_{j,B} \right] + h.c.,$$

(2)

where $t_B = 2\lambda_0 - t'$, $t'_B = \lambda_0$ with $\lambda_0 = t^2/(D + 2V)$. For most of our calculations, we will either fix $t' = 0$ or $t' = \lambda_0$.

The correlated hopping also includes two terms

$$H_{\text{ch}} = \sum_{ijk \in \square} \lambda_1 c_{i,B}^\dagger c_{j,B} n_{k,B} + \sum_{ijkl \in \square} \frac{\lambda_2}{2} c_{i,B}^\dagger c_{j,B} n_{k,B} n_{l,B}$$

(3)

The combinations ijk and $ijkl$ are summed over all possible ordered vertices of plaquettes in the B sublattice, e.g., 1,2,3,4 in Fig. 1(a1). Finally, there are two-, three-, and four-body density interactions,

$$H_U = \sum_{\langle ij \rangle} 2U_2 n_{i,B} n_{j,B} + \sum_{\langle\langle ij \rangle\rangle} U_2 n_{i,B} n_{j,B} +$$
$$\sum_{[ijk] \in \square} U_3 n_{i,B} n_{j,B} n_{k,B} + \sum_{[ijkl] \in \square} U_4 n_{i,B} n_{j,B} n_{k,B} n_{l,B},$$

(4)

The combinations $[ijk]$ and $[ijkl]$ are summed over all possible unordered vertices of plaquettes in the B sublattice. The four-body interaction U_4 remains repulsive in the full parameter region, while other interaction terms turn from repulsion to attraction when increasing across $V/D = 1$.

The dispersion of the kinetic part H_{hopping} depends on the next-to nearest hopping t'. At $t' = 0$ (shown in the left panel of Fig. 2), the band minimum is located along the boundary of the Brillouin zone. The Fermi surface is connected and has an approximate rotation symmetry. By tuning t' such that $|t'_B/t_B| > 0.5$, two band minima appear at $(0, \pm\pi)$ and $(\pm\pi, 0)$ respectively, where the unit of the wave vectors is $1/a$. The low-energy physics is then controlled by these two valleys which are interchanged under a $\pi/2$ rotation. When tuning to higher dopings, the Fermi surface includes the Van Hove singularities. They are located at $(q, \pm q)$, with q depending on t_B/t'_B. The two-valley low-energy physics is replaced by the one exhibiting new instabilities driven by the larger density of states.

Two-valley continuum theory of the square lattice model. — To construct the continuum theory in the case with two valleys, the degrees of freedom for doped electrons can be decomposed into two valleys: $c_j = \sum_\sigma a \exp[i\mathbf{K}_\sigma \cdot \mathbf{r}_j] \psi_\sigma(\mathbf{r}_j)$ with $\mathbf{K}_+ = (0, \pi)$, $\mathbf{K}_- = (\pi, 0)$, where the fields $\psi_\sigma(\mathbf{r})$ vary slowly at the scale of a, minimal distance between two B-sublattice sites.

At low dopings, we ignore the three- and four-body interactions in H_U. The continuum Hamiltonian includes a kinetic part with anisotropic masses
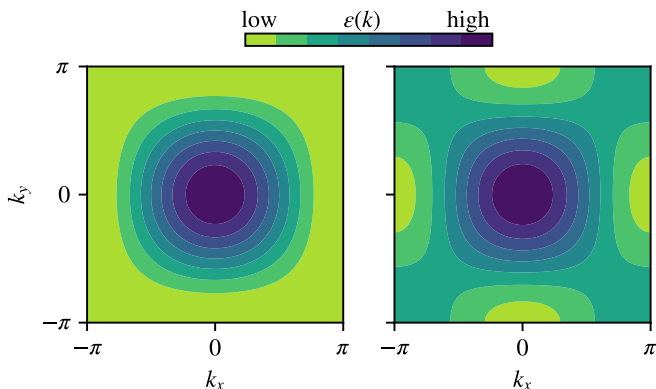
FIG. 2. **Band structures of the square lattice's effective model's kinetic part.** Left: $t' = 0$; Right: $t' = \lambda_0$. The right band structure has two valleys at $(0, \pm\pi)$ and $(\pm\pi, 0)$ respectively. The two-valley structure is absent for $t' = 0$ (left).

$\sum_\sigma \psi_\sigma^\dagger \partial_x^2 \psi_\sigma / (2m_\sigma^{xx}) + \psi_\sigma^\dagger \partial_y^2 \psi_\sigma / (2m_\sigma^{yy})$ at two valleys and a two-body interaction term. There are two contributions to the two-body interaction in the continuum limit, the correlated hopping terms in Eq. (3) and the two-body repulsion terms Eq. (4). In the long wavelength limit, the interaction can be written as

$$\int d^2\mathbf{r} g \psi_+^\dagger(\mathbf{r}) \psi_+(\mathbf{r}) \psi_-^\dagger(\mathbf{r}) \psi_-(\mathbf{r}), \qquad (5)$$

where $g = (16U_2 - 32\lambda_1)a^2 = 16a^2[-4t^2/(D + 3V) + 8t^2(D+2V) - 4t^2/(D+3V)] < 0$; indicating two-particle ground states are always inter-valley bound states. A possible low-doping superconducting (SC) state arises from a condensate of inter-valley pairing $\langle \psi_+(\mathbf{r})\psi_-(\mathbf{r})\rangle \neq 0$. In terms of microscopic fields, we find a total momentum (π, π) $d_{x^2-y^2}$ pairing with an order parameter $\langle c_i c_j \rangle = [(-1)^{i_x+j_y} - (-1)^{i_y+j_x}]\Delta(i - j)$, where Δ is odd under a $\pi/2$ rotation. For finite doping, realizing pairing with (π, π) center-of-mass momentum is frustrated by the shape of the Fermi surfaces. This could lead to a transition to incommensurate (not observed) or other SC phases. The intra-valley interaction is momentum dependent. It turns out that the correlated hopping in the projected model can induce bare attractive interaction between pairs of fermion modes on Fermi surface with zero net momentum (details see the supplement [27]). It is also possible that getting close to the Van Hove singularity can promote attraction. Thus, a possibility of intra-valley pairing, likely p-wave, is suggested.

Binding energies for few-particle doping. — Next, we show our numerical results of pair and larger bound states formation in the dilute doping limit. Binding energies can be deduced from the difference of 1-particle doping energy and energy per particle of n-particle doping; the data for the effective model ($D/t = \infty$) are plotted in Fig. 3. (Our data for $D/t = 5, 10$ can be found in Ref. [27].) From the data, we can infer that at $D/t = \infty$, there can be a stable dilute pairing phase for the hon-

eycomb lattice with $V/D \lesssim 1$. The pairing phase is not favored for the square lattice with $t' = 0$; but it can exist with $t' > 0$. For $t' = \lambda_0$, the condition for pairing phase is $V/D \lesssim 0.6$.

We also determine the momenta of the few-particle ground states. The momentum of a pair for the square lattice with $t' = \lambda_0$ and the honeycomb lattice, are respectively (π, π) and $(0, 0)$. Recall that two valleys of the honeycomb lattice are located at $\pm\mathbf{K}$ (standard notation [28]), and those of the square lattice model are located at $(\pi, 0)$ or $(0, \pi)$. This along with finite pair binding energy results indicates a inter-valley pairing mechanism and explains the absence of it in the case of $t' = 0$ with the absence of valleys. The two-valley structure provides a mechanism for the formation of the bound state possible for pair and also prohibitive for larger bound states, with the condition that the attraction is sufficient for binding exists only between fermions in different valleys. The later condition can be usually met with weak coupling as the intra-valley coupling is less relevant in the dilute doping limit.

Numerical study of the quantum phases at finite doping. — The above few-body and continuum theory results provide an indication of superconductivity at low doping and its instability with respect to large interaction. In the following, we apply DMRG and FRG to infer the quantum phases of the full models with $D = 10$ at finite fermion doping from weak to strong coupling (details see the supplement [27]); the results are summarized in Fig. 1. The $d_{x^2-y^2}$-and f-wave superconductivity of square and honeycomb lattice expected at dilute doping are observed by both methods. Upon increasing doping the square lattice by ~ 0.1, our FRG calculation indicates a $p+ip$ superconducting phase. In the honeycomb lattice model, the f-wave superconductivity persists for larger doping, corroborating the main claim of Ref. [9, 11]; but our DMRG data suggest the absence of superconductivity at the Van Hove singularity $\nu = 1/4$, in contrast to Ref. [9, 11]. Recall that near the Van Hove singularity the two-valley picture breaks down.

In the weak coupling regime ($V/D \lesssim 0.3$), we perform FRG calculations [23, 29] at the one-loop level. We only include the static self-energy and the static effective interaction. The inclusion of the static self-energy has been shown to cover already the relevant physics in disordered systems [30], here taking care of possible further increase of the band-gap. For our simulations we use the TU^{2}FRG [31] which has been demonstrated to fulfill in the FRG equivalence class [32]. We distinguish different phases in our FRG simulations by inspection of the eigenvectors corresponding to the largest eigenvalue of each diagrammatic channel. Each of these channels corresponds to a different type of instability and the symmetry of the eigenvector gives the symmetry of the ordering. The Fourier transformation of these eigenvectors at the B-sublattice are visualized as insets in Fig. 1. In the strong coupling regime ($V/D \gtrsim 0.5$), we use DMRG [21, 22] to obtain ground states on infinite cylinder geometry [33].
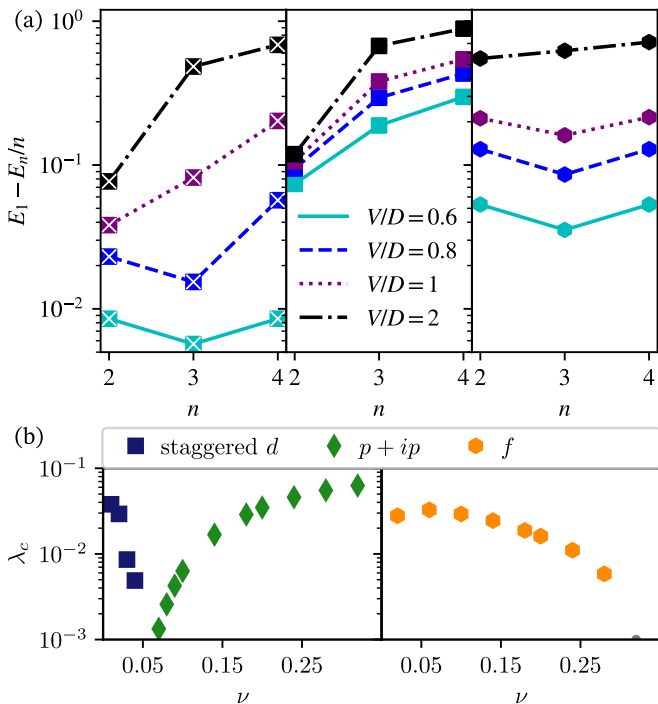
FIG. 3. **Results from exact diagonalization (ED) in the effective model for few-particle doping and FRG in the full model for finite doping.** (a) Energy per particle of the n-particle ground states; the unit is t^2/D. Calculations are performed for the effective models using ED with finite-size extrapolation. From left to right are the square lattice model with $t' = \lambda_0$ and $t' = 0$ and the honeycomb lattice. Finite $E_1 - E_2/2$ indicates the existence of two-particle bound states. Paired phases near the dilute limit is indicated by that the energy per particle $E_1 - E_m/(m)$ is a constant for every positive even m and larger than the values for odd m. On the other hand, if there is some n, $E_1 - E_n/n$ greater than $E_1 - E_2/2$, larger bound states are favoured. (b) FRG predicted phases and energy scales λ_c in units of t^2/D. On the left side, the square lattice model with $t' = \lambda_0$ and on the right the honeycomb lattice is shown. We choose $V = 2t$ as interaction.

We consider cylinders with up to 8 sites along the circumference. The counterpart of 2D superconductivity on the cylinder cannot retain long-range order because of the Mermin-Wagner theorem. But the pair correlation is expected to be dominant over single-particle correlation. In most common cases, the single-particle excitation of a quasi-1D system is fully gapped, see e.g. Ref. [34]; the single particle correlation length ξ_1 is finite while the pair correlation length ξ_2 can diverge. Thus, an observation of estimated $\xi_2 \gg \xi_1$ serves as evidence for such pairing. The DMRG estimation usually sets lower bounds for correlation lengths, which become tighter for increasing the number of variational parameters characterized by bond dimension χ [35].

For the square lattice, we find the predicted $d_{x^2-y^2}$-wave superconductor at small doping within our FRG simulations with $t' = \lambda_0$. However, the critical energy scale drops rapidly upon increasing doping and at larger doping ($\nu \approx 0.1$) we observe a transition to a $p_x + ip_y$ topological superconductor with Chern number [36] $\mathcal{C} = 2$. The transition between the phases seems to be driven by a change of weight within the particle-particle loop, where upon doping the $d_{x^2-y^2}$ eigenvector will be increasingly suppressed while the p_x/p_y pair will increase in strength. At stronger interactions ($V/D \approx 0.25$) our FRG breaks down, manifested as a linear ramp up of the density-density interaction. This ramp up marks the breakdown of the perturbative regime and hence FRG cannot be used to examine the phases. We additionally study the case $t' = 0$ for which the two valleys are absent, the ramp-up problem exists at low dopings even for weak interaction and a $\mathcal{C} = 1$ $p + ip$ is observed for some larger dopings [27]. From the DMRG data ($V/D \gtrsim 0.5$, $t' = \lambda_0$), a finite single-particle correlation length ξ_1 is only consistently found in small doping $\sim 1/64$ and intermediate interaction; in this case, the pair correlation shows a dominant oscillatory part, supporting the staggered $d_{x^2-y^2}$ pairing. For larger doping, no evidence of convergent ξ_1 is found and no evidence for time-reversal symmetry breaking is found for the implemented larger bond dimensions. While these can be features of a quasi-1-D analogue of a Fermi liquid (FL), topological $p + ip$ pairing cannot be excluded. The particle-number-conserved 1D analogue of topological p-wave state has been suggested to be adiabatically connected to an FL [37]; a deeper understanding to quasi-1-D analogue of $p + ip$ is needed to better interpret the data for the $p + ip$ SC or FL region of Fig. 1(b1). The region for large V/D denoted as DW in Fig. 1, is characterized by inhomogeneous densities within the implemented bond dimensions. The 2D phases are speculated to be charge density waves at sufficient commensurate dopings; other dopings could be Fermi liquids or phases separated by Maxwell construction. The density wave patterns are difficult to determine as they may only fit on larger cylinders than studied.

For the honeycomb lattice, we observe f-wave superconductivity in FRG for a broad range of doping, which exceeds Van Hove doping $1/4$. The range is slightly smaller than an RPA result Ref. [11]. Similar to the square lattice, there is also a ramp-up refraining FRG prediction at stronger coupling. Our DMRG for stronger coupling shows a broad range for pairing with a single-particle gap. However, right at the Van Hove doping $\nu = 1/4$, most cylinder setups including the largest, point to insulating states [27]. The CL indicates the collapse of fermions leaving part of the system with vanishing occupancy on the B sublattice; collapses are usually observed for models with strong attractive interactions [19, 38, 39].

Discussion.— We examined fermion pairing driven by repulsive interaction and a strong sublattice potential for square lattices and honeycomb lattices. The honeycomb lattice is confirmed to show f-wave pairing, which can be interpreted as inter-valley pairing. The square lattice's counterpart of inter-valley pairing is found to give

a low-doping d-wave superconductivity with (π, π) total momentum. Upon increasing doping, a $p+ip$ topological superconductivity is found. Because of the role and existence condition of valleys, the square lattice model with next-nearest-neighbor hopping can exhibit an asymmetry for electron and hole doping. As an outlook, one may also include spin degrees of freedom [10, 40] and more types of interactions and hoppings, which serves as extensions of ionic Hubbard models [41–43]. This may have implications for real materials and provide possibility of the sought-after $p+ip$ superconductivity with topological order.

[1] W. Kohn and J. M. Luttinger, New mechanism for superconductivity, Phys. Rev. Lett. **15**, 524 (1965).

[2] P. A. Lee, N. Nagaosa, and X.-G. Wen, Doping a Mott insulator: Physics of high-temperature superconductivity, Rev. Mod. Phys. **78**, 17 (2006).

[3] M. R. Norman, The Challenge of Unconventional Superconductivity, Science **332**, 196 (2011).

[4] G. R. Stewart, Unconventional superconductivity, Advances in Physics **66**, 75 (2017).

[5] J. Bardeen, L. N. Cooper, and J. R. Schrieffer, Theory of Superconductivity, Phys. Rev. **108**, 1175 (1957).

[6] W. A. Little, Possibility of Synthesizing an Organic Superconductor, Phys. Rev. **134**, A1416 (1964).

[7] X. Chen, S. Maiti, A. Linscheid, and P. J. Hirschfeld, Electron pairing in the presence of incipient bands in iron-based superconductors, Phys. Rev. B **92**, 224514 (2015).

[8] Z. Dong and L. Levitov, Activating superconductivity in a repulsive system by high-energy degrees of freedom, arXiv preprint arXiv:2103.08767 (2021).

[9] V. Crépel and L. Fu, New mechanism and exact theory of superconductivity from strong repulsive interaction, Science Advances **7**, eabh2233 (2021).

[10] V. Crépel and L. Fu, Spin-triplet superconductivity from excitonic effect in doped insulators, Proceedings of the National Academy of Sciences **119**, e2117735119 (2022).

[11] V. Crépel, T. Cea, L. Fu, and F. Guinea, Unconventional superconductivity due to interband polarization, Phys. Rev. B **105**, 094506 (2022).

[12] Y. Nakagawa, Y. Kasahara, T. Nomoto, R. Arita, T. Nojima, and Y. Iwasa, Gate-controlled BCS-BEC crossover in a two-dimensional superconductor, Science **372**, 190 (2021).

[13] V. Fatemi, S. Wu, Y. Cao, L. Bretheau, Q. D. Gibson, K. Watanabe, T. Taniguchi, R. J. Cava, and P. Jarillo-Herrero, Electrically tunable low-density superconductivity in a monolayer topological insulator, Science **362**, 926 (2018).

[14] E. Sajadi, T. Palomaki, Z. Fei, W. Zhao, P. Bement, C. Olsen, S. Luescher, X. Xu, J. A. Folk, and D. H. Cobden, Gate-induced superconductivity in a monolayer topological insulator, Science **362**, 922 (2018).

[15] S. Zhang, M. Tanaka, E. Watanabe, H. Zhu, K. Inumaru, and S. Yamanaka, Superconductivity of alkali metal intercalated TiNBr with α-type nitride layers, Superconductor Science and Technology **26**, 122001 (2013).

[16] M. Sigrist and K. Ueda, Phenomenological theory of unconventional superconductivity, Rev. Mod. Phys. **63**, 239 (1991).

[17] M. Cheng, K. Sun, V. Galitski, and S. Das Sarma, Stable topological superconductivity in a family of two-dimensional fermion models, Phys. Rev. B **81**, 024504 (2010).

[18] S. Hesselmann, D. D. Scherer, M. M. Scherer, and S. Wessel, Bond-ordered states and f-wave pairing of spinless fermions on the honeycomb lattice, Phys. Rev. B **98**, 045142 (2018).

[19] K.-H. Ma and N.-H. Tong, Interacting spinless fermions on the square lattice: Charge order, phase separation, and superconductivity, Phys. Rev. B **104**, 155116 (2021).

[20] N. Gneist, D. Kiese, R. Henkel, R. Thomale, L. Classen, and M. M. Scherer, Functional renormalization of spinless triangular-lattice fermions: n-patch vs. truncated-unity scheme (2022).

[21] S. R. White, Density matrix formulation for quantum renormalization groups, Phys. Rev. Lett. **69**, 2863 (1992).

[22] I. P. McCulloch, Infinite size density matrix renormalization group, revisited, arXiv preprint arXiv:0804.2509 (2008).

[23] W. Metzner, M. Salmhofer, C. Honerkamp, V. Meden, and K. Schönhammer, Functional renormalization group approach to correlated fermion systems, Rev. Mod. Phys. **84**, 299 (2012).

[24] N. Read and D. Green, Paired states of fermions in two dimensions with breaking of parity and time-reversal symmetries and the fractional quantum hall effect, Phys. Rev. B **61**, 10267 (2000).

[25] A. H. MacDonald, S. M. Girvin, and D. Yoshioka, $\frac{t}{U}$ expansion for the Hubbard model, Phys. Rev. B **37**, 9753 (1988).

[26] A. L. Chernyshev, D. Galanakis, P. Phillips, A. V. Rozhkov, and A.-M. S. Tremblay, Higher order corrections to effective low-energy theories for strongly correlated electron systems, Phys. Rev. B **70**, 235111 (2004).

[27] See Supplemental Material at XXX.

[28] A. H. C. Neto, F. Guinea, N. M. R. Peres, K. S. Novoselov, and A. K. Geim, The electronic properties of graphene, Reviews of Modern Physics **81**, 109 (2009).

[29] N. Dupuis, L. Canet, A. Eichhorn, W. Metzner, J. Pawlowski, M. Tissier, and N. Wschebor, The nonperturbative functional renormalization group and its applications, Physics Reports **910**, 1 (2021).

[30] L. Markhof, B. Sbierski, V. Meden, and C. Karrasch, Detecting phases in one-dimensional many-fermion systems with the functional renormalization group, Physical Review B **97**, 10.1103/physrevb.97.235126 (2018).

[31] J. B. Hauck and D. M. Kennes, TU^{2}FRG: a scalable approach for truncated unity functional renormalization group in generic fermionic models, The European Physical Journal B **95**, 10.1140/epjb/s10051-022-00316-x (2022).

[32] J. Beyer, J. B. Hauck, and L. Klebl, Reference results for the momentum space functional renormalization group, The European Physical Journal B **95**, 10.1140/epjb/s10051-022-00323-y (2022).

[33] S. B. Sinnott and R. Andrews, Carbon nanotubes: Synthesis, properties, and applications, Critical Reviews in Solid State and Materials Sciences **26**, 145 (2001).

[34] C. Peng, Y. Wang, J. Wen, Y. Lee, T. Devereaux, and H.-C. Jiang, Enhanced superconductivity by near-neighbor attraction in the doped hubbard model, arXiv preprint arXiv:2206.03486 (2022).

[35] F. Pollmann, S. Mukerjee, A. M. Turner, and J. E. Moore, Theory of Finite-Entanglement Scaling at One-Dimensional Quantum Critical Points, Phys. Rev. Lett. **102**, 255701 (2009).

[36] T. Fukui, Y. Hatsugai, and H. Suzuki, Chern numbers in discretized brillouin zone: Efficient method of computing (spin) hall conductances, Journal of the Physical Society of Japan **74**, 1674 (2005).

[37] C. L. Kane, A. Stern, and B. I. Halperin, Pairing in Luttinger Liquids and Quantum Hall States, Phys. Rev. X **7**, 031009 (2017).

[38] Y. He, B. Tian, D. Pekker, and R. S. K. Mong, Emergent mode and bound states in single-component one-dimensional lattice fermionic systems, Phys. Rev. B **100**, 201101 (2019).

[39] L. Gotta, L. Mazza, P. Simon, and G. Roux, Pairing in spinless fermions and spin chains with next-nearest neighbor interactions, Phys. Rev. Research **3**, 013114 (2021).

[40] Long-Yun Xiao and Shun-Li Yu and Wei Wang and Zi-Jian Yao and Jian-Xin Li, Possible singlet and triplet superconductivity on honeycomb lattice, EPL (Europhysics Letters) **115**, 27008 (2016).

[41] M. Messer, R. Desbuquois, T. Uehlinger, G. Jotzu, S. Huber, D. Greif, and T. Esslinger, Exploring Competing Density Order in the Ionic Hubbard Model with Ultracold Fermions, Phys. Rev. Lett. **115**, 115303 (2015).

[42] K. Bouadim, N. Paris, F. Hébert, G. G. Batrouni, and R. T. Scalettar, Metallic phase in the two-dimensional ionic Hubbard model, Phys. Rev. B **76**, 085112 (2007).

[43] T. Watanabe and S. Ishihara, Band and Mott Insulators and Superconductivity in Honeycomb-Lattice Ionic-Hubbard Model, Journal of the Physical Society of Japan **82**, 034704 (2013).

[44] P. Weinberg and M. Bukov, QuSpin: a Python Package for Dynamics and Exact Diagonalisation of Quantum Many Body Systems. Part II: bosons, fermions and higher spins, SciPost Phys. **7**, 20 (2019).

[45] J. Hauschild and F. Pollmann, Efficient numerical simulations with Tensor Networks: Tensor Network Python (TeNPy), SciPost Phys. Lect. Notes , 5 (2018).

[46] Jülich Supercomputing Centre, JURECA: Data Centric and Booster Modules implementing the Modular Supercomputing Architecture at Jülich Supercomputing Centre, Journal of large-scale research facilities **7**, 10.17815/jlsrf-7-182 (2021).

I. SUPPLEMENTAL MATERIAL

A. Schrieffer-Wolff transformation

The ground state at filling $n = 1$ is given by all A sites occupied. We use the Schrieffer-Wolff transformation to find the low-energy physics when extra electrons are brought in by doping. The Hamiltonian is comprised of a kinetic part H_k which creates high-energy excitation and an interaction part H_U which controls the zero-doping state. The Schrieffer-Wolff transformation is to eliminate the high-energy kinetic Hamiltonian order by order through a unitary transformation $\exp(iS)$

$$H' = e^{iS} H e^{-iS} = H + [iS, H] + \frac{1}{2}[iS, [iS, H]] + \dots. \tag{S1}$$

The transformation operator is expanded in the order of t/V or t/U, $S = S^1 + S^{(2)} + \dots$. For this purpose, we decompose the kinetic Hamiltonian into the terms preserving the interaction $H_{00}^{(0)}$ and those creating higher energy excitations $\tilde{H}_k$. The aim of $S^{(1)}$ is to eliminate those components $\tilde{H}_k$

$$[iS^{(1)}, H_U] = -\tilde{H}_k, \quad H_k = H_{00}^{(0)} + \tilde{H}_k \text{ and } [\tilde{H}_k, H_U] \neq 0, [H_{00}^{(0)}, H_U] = 0 . \tag{S2}$$

The SW transformed Hamiltonian to the order of t^2/U is given by the sum $[iS^{(1)}, H_k] + [iS^{(1)}, [iS^{(1)}, H_U]]/2 = [iS^{(1)}, \tilde{H}_k]/2 + [iS^{(1)}, H_{00}^{(0)}]$. The effective theory is obtained by projecting this expression to the state with A occupied.

In order to obtain $S^{(1)}$, it is more convenient to decompose H_k into different ladder operators of the onsite potential and the nearest-neighbor repulsion. We do this first for the hopping process from A to B site. It increases the onsite potential by D. The nearest-neighbor repulsion brought by this process depending on the number of neighbors of A and B, $\delta E = (n_B - n_A)V$. With these observations, the kinetic Hamiltonian is decomposed as

$$
H_k = \left(H_{00}^{(0)} + H_A \right) + \left(\sum_{m,n} H_{m,n}^+ + H_{m,n}^- \right)
$$
$$
= \left(t' \sum_{ij} c_{i,B}^\dagger c_{j,B} + t' \sum_{ij} c_{i,A}^\dagger c_{j,A} \right) + \left(t \sum_{j,r,m,n} P_{m,j+r}^B c_{j+r,B}^\dagger c_{j,A} P_{n,j}^A + t \sum_{j,r,m,n} P_{m,j-r}^A c_{j-r,A}^\dagger c_{j,B} P_{n,j}^B \right), \quad \text{(S3)}
$$

where the next-nearest-neighbor hopping include terms preserving H_U and those connecting states with different distribution of A particles. The operators $P_{m,j}^{A/B}$ are projection into the state where the particle A/B at unit cell j has m neighbors occupied. They can be written in terms of of the sum over the product operators $\prod_r n_r \prod_{r'} (1 - n_{r'})$, where r, r' are the occupied/unoccupied neighbors. Notice that m, n cannot be larger than $N - 1$, where N is the number of nearest neighbors in this lattice, as the hopping operators in the middle of Eq. (S3) always eliminate one neighbor. One can verify the following commutation relations

$$
[H_U, H_{m,n}^\pm] = [\pm D + (m - n)V] H_{m,n}^\pm. \quad \text{(S4)}
$$

With these relation, we can define the leading order transformation for the AB hopping to be

$$
iS_{AB}^{(1)} = \sum_{m,n} \frac{H_{m,n}^+}{D + (m - n)V} - \frac{H_{m,n}^-}{D - (m - n)V}. \quad \text{(S5)}
$$

Such similar expressions $S_{AA}^{(1)}, S_{BB}^{(1)}$ can also be obtained for the AA, BB hopping with different numbers of neighbors occupied. So $S^{(1)}$ is comprised of operators that create excitations of H_U. The observation is that those $S_{AA}^{(1)}, S_{BB}^{(1)}$ terms annihilate the state with all A sites occupied. So their contribution to the second order expansion $[iS^{(1)}, \tilde{H}_k]/2$ vanishes after the projection. What are left are terms diagonal in H_U. The resulting expression $[iS^{(1)}, H_{00}^{(0)}] \simeq t't/U$ is off-diagonal in the ground state of H_U. It will be further eliminated to the order $1/U^2$ by the second-order SW transformation. So we can neglect it at the order of $1/U$. The Hamiltonian is simplified to a quadratic form of $H_{m,n}^\pm$. As the low energy physics is obtained by projecting H' to the state with all A sites occupied, this requires the total excitation should have equal number of $+$ and $-$ and the sum of $m - n$ should vanish. As $H_{m,n}^-$ annihilates the low-energy manifold, it ends up with the following equation

$$
H'_{\text{eff}} = -\sum_{m',n} \frac{H_{m',m'+N-n}^- H_{N,n}^+}{D + (N - n)V}. \quad \text{(S6)}
$$

As the occupation on site A must be conserved, there are two situations in the above summation. When the bond operators in $H_{m',m'+N-n}^-$ and $H_{N,n}^+$ are taking the same one, we obtain density interaction terms. When they differs, we have hopping terms for B fermions. It is more convenient to write out the Hamiltonian for the four neighbors around one A site. Choosing (i, j, k, l) to be the four neighbors of a particle A, we have the following terms for the density interaction part

$$
H_4^U = -\frac{4t^2}{D + 3V} (1 - n_i)(1 - n_j)(1 - n_k)(1 - n_l), \quad \text{(S7)}
$$

$$
H_3^U = -\frac{3t^2}{D + 2V} (1 - n_i)(1 - n_j)(1 - n_k)n_l + \text{PM}, \quad \text{(S8)}
$$

$$
H_2^U = -\frac{2t^2}{D + V} (1 - n_i)(1 - n_j)n_k n_l + \text{PM}, \quad \text{(S9)}
$$

$$
H_1^U = -\frac{t^2}{D} (1 - n_i)n_j n_k n_l + \text{PM}, \quad \text{(S10)}
$$

where PM means *distinct* combinations obtained by permuting i, j, k, l. For the hopping processes from $i \to j$, we need that the A particle has neighbor i occupied before the hopping and j occupied after the hopping. These terms

are given by

$$H_3^k = \frac{t^2}{D+2V} c_{i,B}^\dagger c_{j,B}(1-n_k)(1-n_l) + \text{PM}, \tag{S11}$$

$$H_2^k = \frac{t^2}{D+V} c_{i,B}^\dagger c_{j,B} n_k(1-n_l) + \text{PM}, \tag{S12}$$

$$H_1^k = \frac{t^2}{D} c_{i,B}^\dagger c_{j,B} n_k n_l + \text{PM}. \tag{S13}$$

Similarly, PM means *distinct* combinations obtained by permuting i,j,k,l

Now we collect the contributions together. We have two-body, three-body and four-body interactions:

$$H'_{U,\text{eff}} = \sum_{ij} U_2 n_i n_j + \sum_{ijk} U_3 n_i n_j n_k + \sum_{ijkl} U_4 n_i n_j n_k n_l. \tag{S14}$$

The summation of i,j,k,l is defined by counting the different two-, three- and four-combinations of the neighbors around every A site. So the two-body interaction along the diagonal of the square lattice should be counted twice. Their coefficients are given by

$$U_2 = -\frac{2t^2}{D+V} + \frac{6t^2}{D+2V} - \frac{4t^2}{D+3V}, \tag{S15}$$

$$U_3 = -\frac{t^2}{D} + \frac{6t^2}{D+V} - \frac{9t^2}{D+2V} + \frac{4t^2}{D+3V}, \tag{S16}$$

$$U_4 = \frac{4t^2}{D} - \frac{12t^2}{D+V} + \frac{12t^2}{D+2V} - \frac{4t^2}{D+3V}. \tag{S17}$$

The effective hopping Hamiltonian can be assisted by the other two neighbors around each A site

$$H'_{k,\text{eff}} = \sum_{ij} \lambda_0 c_{i,B}^\dagger c_{j,B} + \sum_{ijk} \lambda_1 c_{i,B}^\dagger c_{j,B} n_k + \sum_{ijkl} \lambda_2 c_{i,B}^\dagger c_{j,B} n_k n_l, \tag{S18}$$

where the hopping parameters are

$$\lambda_0 = \frac{t^2}{D+2V} \tag{S19}$$

$$\lambda_1 = \frac{t^2}{D+V} - \frac{t^2}{D+2V} \tag{S20}$$

$$\lambda_2 = \frac{t^2}{D} - \frac{2t^2}{D+V} + \frac{t^2}{D+2V}. \tag{S21}$$

All the parameters as a function of V/D are plotted in Fig. S1.

B. Continuum theory for low dopings

The effective inverse mass tensor at the two valleys are

$$m_\pm^{-1} = a^2 \begin{pmatrix} 4t'_B \mp 2t_B & 0 \\ 0 & 4t'_B \pm 2t_B, \end{pmatrix} \tag{S22}$$

where the subscript $+$ ($-$) denotes the valley located at $(0,\pi)$ $((\pi,0))$. Recall that the two valleys being minimum is given by the condition $|t'_B/t_B| > 0.5$. We see that the mass tensor is diagonal in the coordinate we choose, and there is mass anisotropy for each valley.

We introduce the center-of-mass coordinates: $\delta\mathbf{r} = \mathbf{r}_+ - \mathbf{r}_-$, $\mathbf{R} = \bar{m}_+ \mathbf{r}_+ + \bar{m}_- \mathbf{r}_-$, where $\bar{m}_\pm = m_\pm / \text{Tr}(m_\pm)$. The (first-quantized) kinetic Hamiltonian of the two par-

ticles can be written as $(\nabla_{\delta\mathbf{r}}^T \mu^{-1} \nabla_{\delta\mathbf{r}} + \nabla_{\mathbf{R}}^T M^{-1} \nabla_{\mathbf{R}})/2$. We find that the relative inverse mass tensor μ^{-1} is isotropic: $\mu^{-1} = \mu_0^{-1} I$, where $\mu_0^{-1} = (8a^2 t'_B)$ and I is the 2×2 identity matrix. The continuum approximation of two-particle problem is similar to that of the honeycomb model [9]. The two-particle binding energies can be calculated in the center-of-mass reference frame [9]:

$$E_{\text{bp}} = e_{\text{bp}}[e^{2\pi/(\mu_0|g|)} - 1]/\mu_0, \tag{S23}$$

where $\mu_0 = (8a^2 t'_B)^{-1}$ is the relative mass. The result is independent of the specific value of t_B (t' in the full model) as long as the ground states of single fermion [two fermions] are in the $(0,\pi)$ or $(\pi,0)$ [(π,π)] momentum sector, consistent with the microscopic Hamiltonian
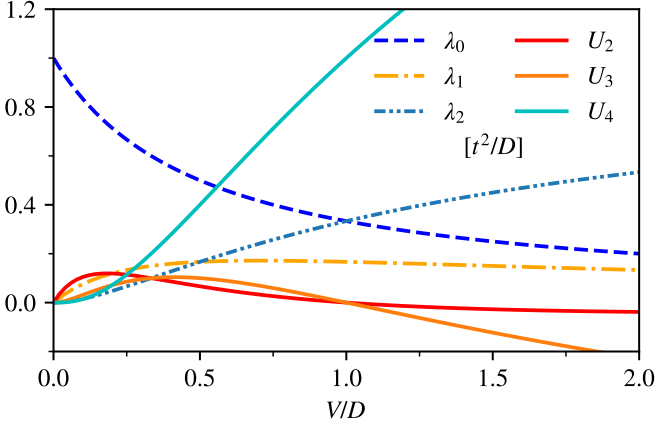
FIG. S1. Parameters of the large-D effective theory of the square lattice model.
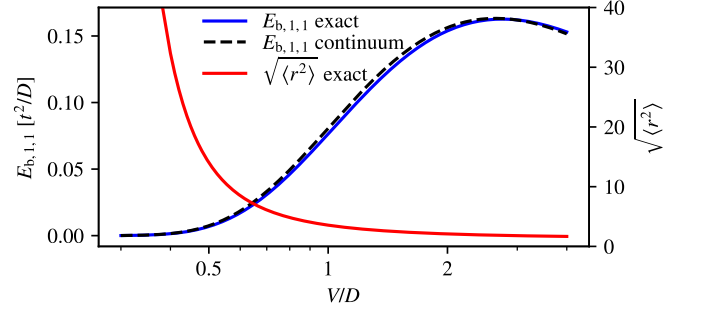

FIG. S2. Binding energies and bound states sizes of two fermions for the effective square lattice model with two valleys. The dashed line denotes the continuum effective theory with one fitting parameter given by matching small V/D data.

being independent of t_B in the two-particle (π, π) sector. We fit e_{bp} using exact data in the small V/D region and plot the continuum effective result together with the exact result in Fig. 3. Different from the honeycomb model, the binding energies will drop for large V, because $|g|$ will decay to zero for large V instead of converging to a constant.

To extract coefficients of interaction in the continuum theory, we write the correlated hopping as

$$\lambda_1 \sum_{i,j,k} c_i^\dagger c_j^\dagger c_j c_k = \lambda_1 \sum_{\substack{i,j,k, \\ \mathbf{k},\mathbf{k}',\mathbf{q},\sigma_i}} \psi_{\sigma_1,\mathbf{k}-\mathbf{q}}^\dagger \psi_{\sigma_2,\mathbf{k}'+\mathbf{q}}^\dagger \psi_{\sigma_3,\mathbf{k}'} \psi_{\sigma_4,\mathbf{k}}$$
$$\times e^{-i(\mathbf{K}_{\sigma_1}+\mathbf{k}-\mathbf{q})\cdot\mathbf{a}_i - i(\mathbf{K}_{\sigma_2}-\mathbf{K}_{\sigma_3}+\mathbf{q})\cdot\mathbf{a}_j}$$
$$\times e^{i(\mathbf{K}_{\sigma_4}+\mathbf{k})\cdot\mathbf{a}_k}, \qquad (S24)$$

where $\mathbf{a}_i$ is taken from the four vectors connecting A to its nearest B neighbours. The variables $\mathbf{k}, \mathbf{q}, \mathbf{k}'$ are taken to be much smaller than $|\mathbf{K}^+ - \mathbf{K}^-|$. Similarly, the repulsion term is rewritten as

$$U_2 \sum_{ij} c_i^\dagger c_j^\dagger c_j c_i = U_2 \sum_{\substack{i,j,\mathbf{q}, \\ \mathbf{k},\mathbf{k}',\sigma_i}} \psi_{\sigma_1,\mathbf{k}-\mathbf{q}}^\dagger \psi_{\sigma_2,\mathbf{k}'+\mathbf{q}}^\dagger \psi_{\sigma_3,\mathbf{k}'} \psi_{\sigma_4,\mathbf{k}}$$
$$\times e^{-i(\mathbf{K}_{\sigma_1}-\mathbf{K}_{\sigma_4}-\mathbf{q})\cdot\mathbf{a}_i - i(\mathbf{K}_{\sigma_2}-\mathbf{K}_{\sigma_3}+\mathbf{q})\cdot\mathbf{a}_j}.$$
$$(S25)$$

The continuum interactions between different valleys and inside the same valley are given by taking appropriate combinations of σ_i and their anti-symmetrized partners.

The result of inter-valley interaction has been given in the main text. Now we consider intra-valley interaction with finite doping. We consider the weak interacting limit and discuss the interaction between modes on Fermi surface of a valley, for example the $+$ valley. Here the momenta are defined as the deviation to $(0, \pi)$. In general we have.

$$\sum_{\mathbf{k},\mathbf{k}',\mathbf{q}} g(\mathbf{k}, \mathbf{k}', \mathbf{q}) \psi_{+,\mathbf{k}-\mathbf{q}}^\dagger \psi_{+,\mathbf{k}'+\mathbf{q}}^\dagger \psi_{+,\mathbf{k}'} \psi_{+,\mathbf{k}} \qquad (S26)$$

We focus on two-particle scattering with net zero deviation to $\mathbf{K}_+$ and small doping (momenta is small enough to perform Taylor expansion).

$$\sum_{\mathbf{q}_1,\mathbf{q}_2} \tilde{g}(\mathbf{q}_1, \mathbf{q}_2) \psi_{+,\mathbf{q}_1}^\dagger \psi_{+,-\mathbf{q}_1}^\dagger \psi_{+,-\mathbf{q}_2} \psi_{+,\mathbf{q}_2} \qquad (S27)$$

Set $\mathbf{q}_1 = \mathbf{q}_2$ and $\mathbf{q}_1 = -\mathbf{q}_2$ respectively, we can obtain the density-density interaction, $\propto [2\lambda_1(q_{1,x}^2 - q_{1,y}^2) + U_2(q_{1,x}^2 + q_{1,y}^2)]n_+(\mathbf{q}_1)n_+(-\mathbf{q}_1)$. With the Fermi surface shape close to an eclipse with the long axis along y direction, and $\lambda_1 \approx U_2$ for $V/D < 1$ (Fig. S1), such interaction in most momenta is attractive.

C. Few-particle-doping binding energy with finite D/t

Here, we discuss few-particle-doping binding energies of the full model with finite $D/t = 10, 5$. The binding energies, in the unit of t^2/D are in general smaller for smaller D/t. However, even for $D/t = 5$, we find no substantial difference for inferred stable pairing region, comparing to the effective model with $D/t = \infty$.

As an alternate of binding energy per particle, we represent the results as binding energies for forming bond states with composites. For two-particle and three-particle bond sates, the existence of bond states can be seen from a positive $E_{b,1,1} = 2E_1 - E_0 - E_2$ and $E_{b,1,2} = E_1 + E_2 - E_0 - E_3$ respectively. These quantities are plotted in Fig. S3. Binding energy per particle can be deduced from them. The existence of three-particle is a necessary but not sufficient condition for the criteria we used to infer three-particle bound states are more favoured than pairs. For example. For $V/D = 1$.

Some details of the numerical implementation are as follows. For the full (effective) lattice models, we obtain the ground-state energies E_n of finite systems using DMRG (exact) diagonalization. To accurately compute binding energies, we need system sizes larger than the bound states sizes. We estimate the finite-size errors by doing $1/N$ extrapolation for data of largest two
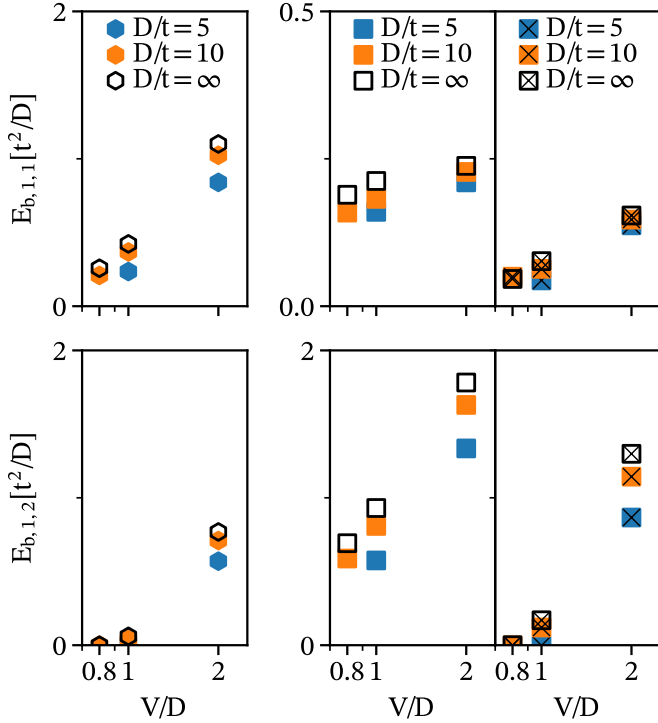
FIG. S3. Binding energies. The binding energies of two fermions are shown in the first row from left to right for the honeycomb lattice model and the square lattice model without t' term and for $t' = \lambda_0$. Correspondingly, the binding energies for an fermion pair and a fermion to form a three-fermion bound state are shown in the second row. The plot scale of the $E_{b,1,1}$ of square lattice models are smaller than others'.
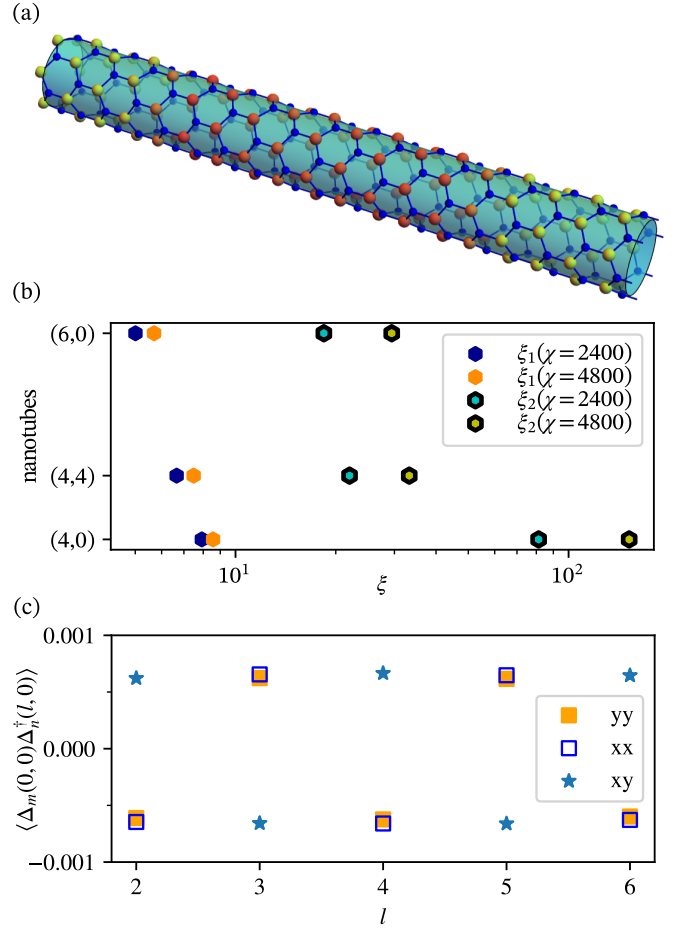

FIG. S4. (a) Cylinder geometry [(6,0) honeycomb nanotube] and a density plot of an inhomogeneous density profile, indicating phase separation. The densities on B sublattice are represented by colors with green for small density and red for larger density. The parameters for the density plot: 1/8 doping, $D = 10, V = 15$ and unit cell size 32; only part of the unit cell is plotted. (b) Correlation length evidence for pairing on infinite cylinder geometry of honeycomb lattice. The indices for nanotubes are standard notations for their sizes and shapes. The ξ_1 (ξ_2) is single-particle (pair) correlation length. For a larger bond dimension χ used in the iDMRG algorithm, a tighter lower bound of ξ is obtained. Here, a smaller $\xi_2(\chi)$ for a larger nanotube is an artifact that the underestimation becomes severer for larger systems if not increasing χ. The other parameters are 1/8 doping, $D = V = 5$. (c) Pair correlation functions for square lattice at 1/64 doping, $V = 6, D = 10$ and tangential direction size 8 unit cell. Definitions of pair operators see the text; the subscripts m, n can be x, y.

systems we obtain. The extrapolated data in Fig. S3 have errors much smaller than the size of marker. The periodic boundary condition is implemented in the exact diagonalization, which enables reading the momentum quantum numbers. DMRG is less efficient to deal with periodic condition along two directions and we thus only implement periodic boundary on one direction while implement open boundary condition on another. In this case, to correctly calculate the bulk binding energy, we find it essential to eliminate the low-energy edge modes. Such modes can be understood by considering the potential and interaction part of the Hamiltonian Eq. 1:$\sum_{\langle i,j \rangle} V n_i n_j + \sum_{i \in B} D n_i$. As A sublattice is almost fully-filled, if a fermion on B sublattice is located at the open boundary rather than in the bulk, it feels less repulsion from the fermions on B sublattice. Consequently, these configurations have lower energy. We find that introducing additional potential terms $V n_i$ on the boundary of B sublattice can eliminate low-energy edge modes.

D. Weak-coupling results

In the weak coupling regime we apply a truncated unity functional renormalization group approach. We a sharp energy cutoff [23], thus the critical energy scale can be interpreted as a critical temperature modulo an unknown scaling factor. We calculate the vertex on a 24×24 mo-
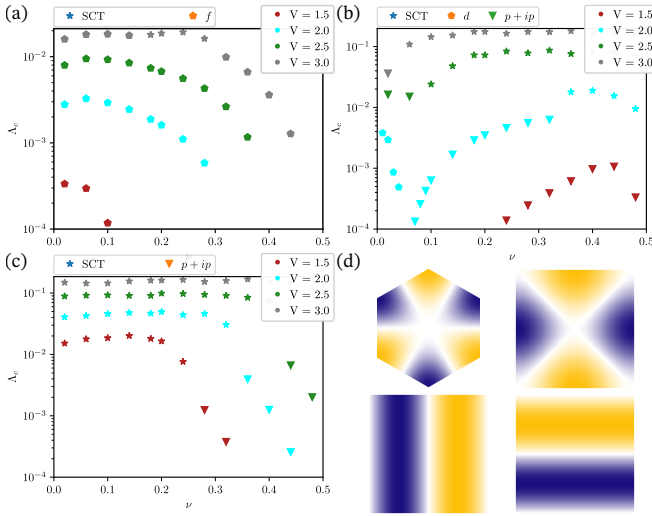
FIG. S5. Results of the FRG simulations for the three different setups and visualisation of the f-wave superconductivity. We abbreviate a flow to strong coupling without divergent susceptibility as SCT, and a divergence of the f-wave component of the pairing susceptibility as f-SC. The y-axis displays the critical energy scale, which is linearly dependent to the critical temperature. The x-axis displays the doping. (a) shows the results for a square lattice with $t' = \lambda_0$ and (b) the square lattice with $t' = 0$ results. (c) shows the results for the honeycomb lattice. In all simulations we kept $D = 10$ and varied V in the given range. (d) visualizes the different superconducting order parameter symmetries encountered, as visualized by the eigenvector of the effective interaction at the orbital at the Fermi level. The upper left shows an f-wave on the honeycomb lattice, the upper right shows a $d_{x^2-y^2}$-wave on the square lattice. The lower two plots correspond to the degenerate pair p_x and p_y with weak admixture of other dependencies.

mentum mesh for both lattices, with a refinement for the bubble integration mesh of 45×45. On the square lattice we include the $25/29$ nearest neighbors in the truncated unity per site within the unit cell for the honeycomb/square lattice. We use a Bogacki–Shampine adaptive integrator for the integration of the flow equations, allowing for a maximal absolute error of 10^{-2} per integration step. The results of the FRG simulations are visualized in Fig. S5. To distinguish different phases, we inspect the behavior of the maximal eigenvalues of each channel during the flow in combination with an inspection of the dominant eigenvectors at the end of the flow. These eigenvectors encode the symmetry and specific type of the instability. In the case of p_y/p_x we find the two eigenvectors to be exactly degenerate. In the real space representation we define $p_{x/y} = \text{sign}(\vec{v}_{x/y} \cdot \vec{d}) \delta_{\vec{v}_{x/y}, \vec{d}}$ with $\vec{v}_x = (1, 0)$, $\vec{v}_y = (0, 1)$ and $\vec{d}$ is the vectorial distance between two sites. To distinguish all possible linear combinations $\cos(\theta)p_x + e^{i\phi}\sin(\theta)p_y$ we perform a single step mean-field calculation and compare the free energy of each starting configuration, as can be seen in Fig. S6.
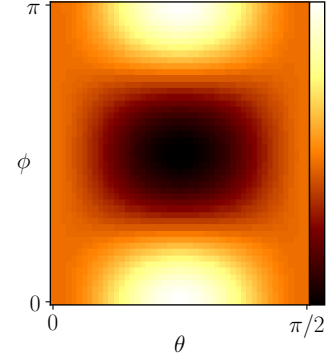

FIG. S6. Free energy minimization in the square lattice with $t' = \lambda_0$, using $\cos(\theta)p_x + e^{i\phi}\sin(\theta)p_y$ as starting values. The combination with the smallest free energy is $\frac{1}{2}(p_x + ip_y)$

To calculate the Chern number in the gapped phase, we employ the method described in Ref. [36].

E. Details of infinite DMRG calculations

We obtain approximate ground states of the Hamiltonian 1 defined on infinite cylinder. We do this by optimizing infinite matrix product states via two-site iDMRG algorithm [22]. We implement the conservation of particle numbers, thus the phase diagram 1 is constructed in terms of doping densities ν. The accuracy of infinite matrix product states can be improved by increasing its bond dimensions (χ, size of the matrices); With efficient optimization, to reach a given accuracy, the required computational resource (e.g. χ) is exponentially large in cylinder circumference. Infinite matrix product states are constructed to be exactly translationally invariant by M lattice unit vector along the axial direction. To implement exact particle number conservation for doping density $\nu = p/q$ (irreducible fraction), M must be integer multiples of q/L_y. (L_y is the number of lattice unit vectors around the cylinder.) To be compatible with possible spontaneous breaking of translational symmetry (e.g., charge density wave state), M has to be compatible with enlarged unit cell. As mentioned in the main text, we estimate of correlation lengths of single-particle and pair to infer superconductivity. We denote them estimated using bond dimension χ as $\xi_1(\chi)$ and $\xi_2(\chi)$ respectively; the larger the bond dimension, the more accurate the estimation.

For the honeycomb lattice model, we study the zigzag and armchair nanotube geometry, denoted as $(n, 0)$ and (n, n) [standard notation [33]] respectively where n characterizes circumference. The $(6, 0)$ nanotube is illustrated in Fig. S4(a). To determine possible pairing gaps as well as competition between states, we limit the cylinder size to $(4, 0), (6, 0), (8, 0)$, and $(4, 4)$ as the data accuracy of interested quantities cannot be reached for larger cylinders. An example of data consistent with fermion

pairing is plotted in Fig. S4(b). As mentioned in the main text, the CL (collapse) region the collapse of fermions leaves part of the system with vanishing occupancy on B sublattice. This is inferred that when increasing iMPS unit cell size, the fermions on B lattice always concentrate on part of the unit cell (see Fig. . S4(a)); the energy also overall decreases for increasing unit cell size. Limited by numbers of unit cell we can implement, this approach cannot exclude charge density waves such as stripes with large unit cell.

For the square lattice, we study the geometry with the axial direction along the shortest lattice unit vector (e.g., that connecting the nodes 1 and 2 in Fig. 1(a1) right). We consider cylinder sizes with 4, 6 and 8 unit vectors along the tangential direction. For 1/64 doping of all cylinders, we find similar behaviors of correlation lengths as the 1/8 doping of honeycomb lattice discussed before (Fig. S4). This already indicates pairing and gapped single-particle excitation. We find evidence for the staggered $d_{x^2-y^2}$ by considering two-point correlations between $\Delta_y(i_x, i_y) = c_{i_x,i_y} c_{i_x,i_y+1}$, $\Delta_y(i_x, i_y) = c_{i_x,i_y} c_{i_x,i_y+1}$ and their Hermitian conjugation. Only the sites on B sublattice are considered. We observe (Fig. S4 (c)) that the sign of $\langle \Delta_x(0,0) \Delta_x^\dagger(l,0) \rangle$ and $\Delta_y(0,0) \Delta_y^\dagger(l,0) \rangle$ oscillates in l; we also observe that the sign of $\langle \Delta_x(0,0) \Delta_x^\dagger(l,0) \rangle$ is opposite to the previous two for a given l.